**ORIGINAL ARTICLE**

# Investigation on microstructure and mechanical properties of the dissimilar lap welding of Al alloy to steel with different filler materials and laser powers

Bin Li[1] · Shanguo Han[2,3] · Wenjun Ao[1] · Yongqiang Yang[2] · Dejia Liu[1,3]

## Abstract

Two types of filler materials, FeCoCrNiMn and Al-10Si-0.3 Mg powder, were utilized to achieve lap welding of 5083 aluminum alloy to DP780 steel using laser deposition welding at various laser powers. By conducting a comparative analysis of the macroscopic morphology, microstructure, hardness, and shear properties of two groups of welded joints, the effects of multi-principal filler material and heat input on the weld formation, microstructure evolution, and shear properties of dissimilar lap joints were evaluated and discussed. An interesting finding was that, compared to the Al-10Si-0.3 Mg powder, the FeCoCrNiMn powder used as filler material had significant advantages in reducing the hardness of the weld zone and improving the shear properties of the lap-welded joints. The multi-principal powder of FeCoCrNiMn was unable to prevent the formation of Fe-Al intermetallic compounds in the weld metal. However, it did alter the elemental compositions and grain morphologies in the weld metal when compared to the Al-10Si-0.3 Mg powder. Moreover, selecting welding parameters with a low heat input was appropriate for the dissimilar metal joining of aluminum to steel using laser deposition welding.

**Keywords** Dissimilar metal joining · Filler material · Microstructure · Shear properties · Hardness · Welding parameters

## 1 Introduction

Automobile lightweight plays a crucial role in reducing energy consumption, saving resources, and mitigating air pollution [1–3]. The utilization of a composite component made of aluminum alloy and high-strength steel is an economically viable and reasonable solution for achieving lightweight automobiles [4, 5]. However, there are two critical factors that make the dissimilar metals welding of aluminum and steel particularly challenging [6–8]. Firstly, the significant differences in thermophysical properties, including the melting point and thermal expansion, between aluminum

---

Bin Li and Shanguo Han contributed equally to the work.

✉ Dejia Liu
   ldj515@126.com

1   School of Materials Science and Engineering, East China Jiaotong University, Nanchang, China

2   School of Mechanical & Automotive Engineering, South China University of Technology, Guangzhou, China

3   Yang Jiang China-Ukraine E. O. PATON Institute of Technology, Yangjiang, China

and steel, result in considerable thermal stress and residual stress within the welded joint. This has a negative impact on the weld formation and the mechanical properties of Al/steel joints. Secondly, based on the Fe-Al binary phase diagram, the maximum solubility of aluminum (Al) in iron (Fe) is limited to 1.285 at.%, while the solubility of Fe in Al is only 0.03 at.%. Consequently, Fe and Al are prone to forming brittle Fe-Al intermetallic compounds (IMCs) during metallurgical reactions. Previous studies have reported that dissimilar welding of aluminum to steel can produce various IMCs, including $Fe_3Al$, $FeAl$, $FeAl_2$, $Fe_2Al_3$, $Fe_2Al_5$, and $FeAl_3$ [9]. The fraction, size, and composition of these IMCs have varying degrees of impact on the weld formation and the mechanical properties of different welded joints. A high fraction of Fe-Al IMCs in the weld zone (WZ) can directly lead to welding failure. Moreover, research has indicated that compared to IMCs rich in Fe, IMCs rich in Al are more brittle and tend to form at the interface between aluminum and steel [9]. This increased brittleness and occurrence at the interface lead to a higher crack sensitivity of the joint [10, 11]. Additionally, reducing the size of IMCs and decreasing the thickness of the IMC layer can help alleviate the degradation in the mechanical properties of the joint. Currently,

effectively controlling the generation and growth of Fe-Al IMCs and reducing defects in the WZ are key challenges in the advancement of aluminum-steel welding technology.

Numerous scholars have conducted extensive research on dissimilar metal welding of aluminum to steel. Previous studies have suggested that welding parameters significantly influence the formation of the WZ and the development of Fe-Al IMCs [12–14]. Three main conclusions can be drawn from these studies: (i) Increased welding heat input leads to higher levels of weld penetration, weld width, and wetting width [15–17]. (ii) The size and quantity of Fe-Al IMCs increase with higher heat input. This is because the high heat input can promote the diffusion of Fe and Al elements, which can facilitate the formation and growth of Fe-Al IMCs [4, 18]. (iii) The combined effects of welding heat input on weld formation and Fe-Al IMCs play a crucial role in determining the mechanical properties of dissimilar metal welded aluminum/steel [12, 19, 20]. Ye et al. [21] pointed out that, due to satisfactory weld formation and a thin interface layer, the tensile strength of dissimilar metal joints exceeded 90% of the aluminum base metal (BM). Yang et al. [22] reported a direct correlation between the tensile strength of laser-welded joints and weld penetration. They found that the optimal joint strength was achieved at a weld penetration of 108 μm. Moreover, as the weld penetration increases, the phase structures may change from iron-rich to brittle aluminum-rich IMCs [22].

However, it should be noted that there is a limit to the improvement in mechanical properties of dissimilar metal joints between aluminum and steel through the optimization of welding parameters. The WZ always contains a specific size and quantity of brittle Fe-Al IMCs. To address this issue, it has been suggested to add elements such as Cu, Ni, Zn, and Si to control the size and number of Fe-Al IMCs [23–25]. Promising results have been achieved using Al-Si and Zn-Al welding wires, as well as Cu and Ni metal interlayers, in dissimilar metal welding of aluminum to steel [26–28]. For example, Wu et al. [28] used a 1.5 mm-thick Cu sheet as an intermediate layer for butt welding aluminum to steel, and no Fe-Al IMCs were detected in the WZ. Xu et al. [29] reported that the shear strength of aluminum-steel lap joints, obtained using a 20 μm Ni foil as the interlayer, was approximately 92% higher than that of joints without the Ni foil. These findings highlight the importance of selecting a suitable filler material for dissimilar metal welding of aluminum to steel.

Recently, the Cantor alloy (FeCoCrNiMn) has emerged as a typical high-entropy alloy [30–32]. It has been identified as a promising filler material for dissimilar metal welding of aluminum to steel. Zhou et al. [33] employed a FeCoCrNiMn sheet as an interlayer to join aluminum and steel, successfully inhibiting the formation of Fe-Al IMCs in the WZ. The study revealed that the strength and plasticity of welded joints improve as the thickness of the IMCs layer decreases from 85 to 30 μm [33]. To expedite the manufacturing process and reduce costs, real-time filling of multi-principal powder through laser deposition welding has been explored. FeCoCrNiMn multi-principal powder was utilized as filler material in the butt welding of 6061 aluminum alloy to 304 stainless steel [34]. The research demonstrated that the utilization of multi-principal filler materials significantly reduced the presence of Fe-Al IMCs in the WZ [34].

As is known, dissimilar metal lap welding of aluminum to steel is widely used in the automotive manufacturing industry. However, there is limited research on lap welding aluminum to steel using multi-principal powder fillers. In this study, the lap welding of 5083 aluminum alloy to DP780 steel was carried out using laser deposition welding, with FeCoCrNiMn multi-principal powder as the filler material. Additionally, Al-10Si-0.3 Mg powder was used as a comparative filler material. Two groups of dissimilar lap joints were fabricated using different laser powers. Comparative analysis was conducted on the macroscopic morphology, microstructure, hardness, and shear properties of the two groups of welded joints. The effects of multi-principal filler material and heat input on the weld formation, microstructure evolution, and mechanical properties of dissimilar lap joints between aluminum and steel were evaluated and discussed.

## 2 Materials and methods

The base materials (BMs) in this study consisted of DP780 steel and 5083 aluminum alloy (AA5083), with dimensions of 120 mm × 100 mm × 1 mm. The multi-principal filler material employed was FeCoCrNiMn powder, which was manufactured by thoroughly blending high-purity elemental metal powders of Fe, Co, Cr, Ni, and Mn. A ball mill was used for the mixing process, operating at a grinding speed of 200 rpm for 2 h. The ball material ratio was 3:1. Additionally, for comparison, commercially available Al-10Si-0.3 Mg powder was utilized.

The dissimilar metals, DP780 steel and AA5083, were lap-welded through laser deposition welding. The welding system consisted of a laser welding head and a TruDisk 10002 disk laser. Caxial powder feeding and single-focus welding methods were employed. The schematic diagram of the laser welding device is shown in Fig. 1, with the steel material positioned on top and the aluminum material on the bottom. To prevent oxidation of the weld seam, argon shielding gas was used. The laser beam was configured to perform Zigzag wobble during the welding process. Two different types of filler materials were utilized namely FeCoCrNiMn and Al-10Si-0.3 Mg powders. The joints welded using FeCoCrNiMn powder were categorized as Group A, and those using Al-10Si-0.3 Mg powder belonged to Group B. A series of welding parameters were utilized for two groups
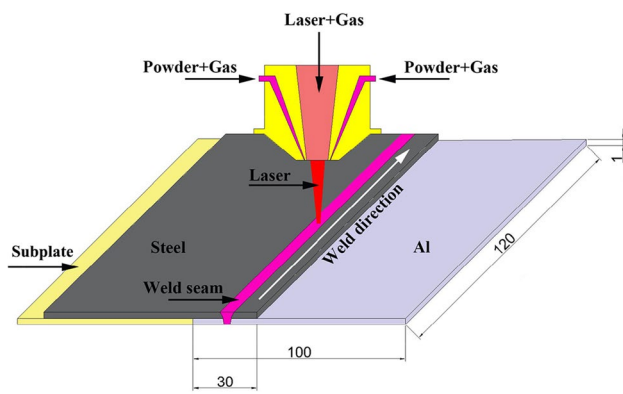
**Fig. 1** Schematic diagram of the weld process

of welded joints. The detailed welding parameters and their corresponding sample numbers can be observed in Table 1.

After welding, metallographic samples were selected from the cross-sections of the welded joints. These samples were etched with an 8 vol% nitric acid-alcohol reagent. Microstructure characterization was conducted using various analytical tools, including an optical microscope (OM), a SU8010 scanning electron microscope (SEM), and an Xflash 6I60 energy-dispersive spectrometer (EDS). The phase structures of the weld metals were examined using the Rigaku SmartLab 9KW X-ray diffraction (XRD). The XRD samples were scanned from 20 to 80° with a step size of 2° utilizing a Cu Kα target. In addition, electron backscatter diffraction (EBSD) was adopted to analyze the microstructure evolution of the weld metals. The EBSD detector employed was an Oxford Symmetry detector, integrated with a Zeiss Gemini 300 SEM. The EBSD data obtained was analyzed using HKL Channel 5 software. Grain boundaries in inverse pole figure (IPF) maps are defined based on a misorientation angle greater than 15°. Furthermore, the shear properties of the welded joints were evaluated using an AG–X

250kN material performance tester, with a displacement rate of 0.5 mm/min. An HV-1000IS Vickers microhardness tester was utilized to evaluate the hardness distribution of the welded joints.

# 3 Results

## 3.1 Macroscopic morphology and shear properties

The surface appearances of the two groups of welded joints are exhibited in Fig. 2. The joints of Group A were welded using FeCoCrNiMn powder, with laser power ranging from 1300 to 1700 W. No obvious welding defects are observed in the appearance of Group A. On the other hand, the joints of Group B were welded using Al-10Si-0.3 Mg powder, with a laser power ranging from 1300 to 1700 W. It should be noted that the joints were not successfully formed when using the Al-10Si-0.3 Mg filler material at a laser power of 1300 W. Additionally, joints formed at laser powers of 1600 W and 1700 W fractured due to cold cracks. The results indicate that both filler materials can be used for the laser deposition welding of AA 5083 and DP780 steel, leading to successful joining with a laser power ranging from 1300 (1350 W) to 1500 W.

Figure 3 indicates that weld collapse is observed in all of the welded joints, which is a common phenomenon in laser welding, as reported in previous studies [17, 35, 36]. As is known, weld collapse is a type of welding defect. The formation of welding defects is closely related to welding parameters and filler materials. To control and mitigate weld collapse, it is crucial to select the appropriate welding parameters, including the laser power and welding speed [17, 35, 36]. Moreover, a gap is found between the steel and aluminum plates. The WZs in the depth direction can be divided into a fusion zone (FZ) and a mixed zone (MZ)

**Table 1** The welding parameters and the corresponding sample numbers of those welded joints

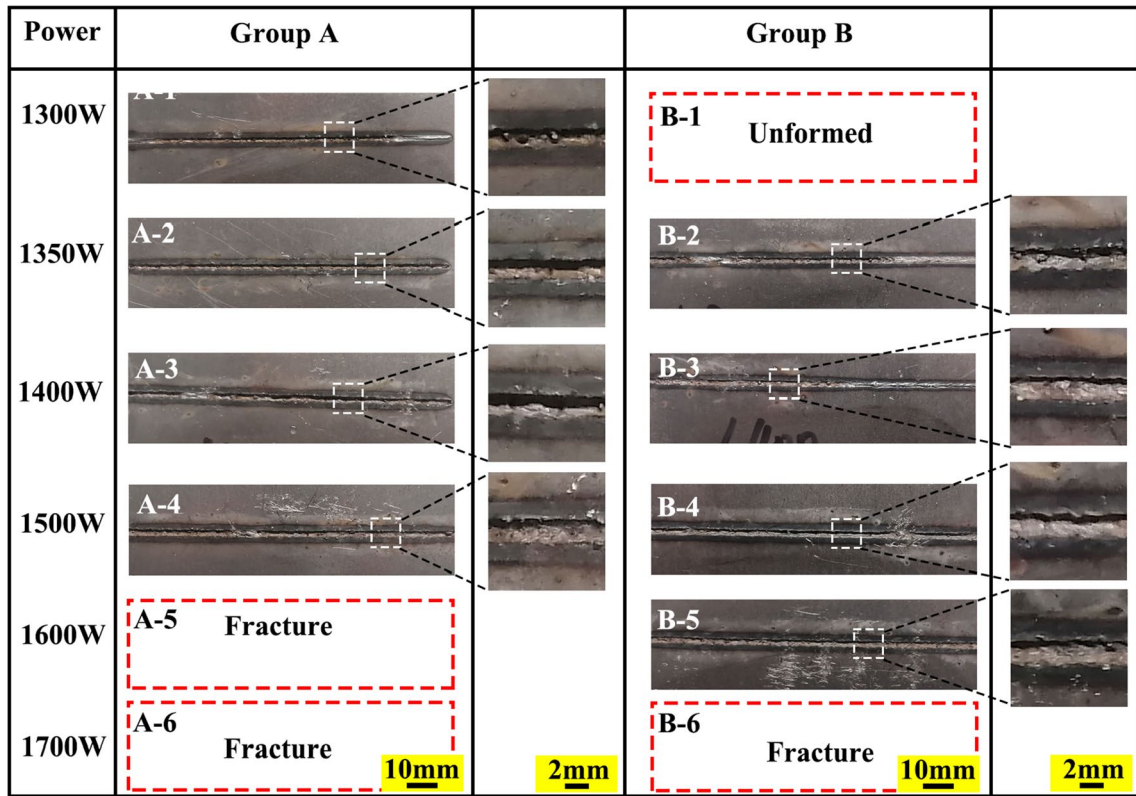| Filler materials | Classification | Sample No | Power (W) | Welding speed (mm/s) | Wobble breadth (mm) | Wobble cycle (s) | Wobble frequency (HZ) |
|---|---|---|---|---|---|---|---|
| FeCoCrNiMn | Group A | A-1 | 1300 | 22 | 1 | 0.786 | 28 |
| | | A-2 | 1350 | 22 | 1 | 0.786 | 28 |
| | | A-3 | 1400 | 22 | 1 | 0.786 | 28 |
| | | A-4 | 1500 | 22 | 1 | 0.786 | 28 |
| Al-10Si-0.3 Mg | Group B | B-1 | 1300 | 22 | 1 | 0.786 | 28 |
| | | B-2 | 1350 | 22 | 1 | 0.786 | 28 |
| | | B-3 | 1400 | 22 | 1 | 0.786 | 28 |
| | | B-4 | 1500 | 22 | 1 | 0.786 | 28 |
| | | B-5 | 1600 | 22 | 1 | 0.786 | 28 |
| | | B-6 | 1700 | 22 | 1 | 0.786 | 28 |

**Fig. 2** The surface appearance of two groups of welded joints
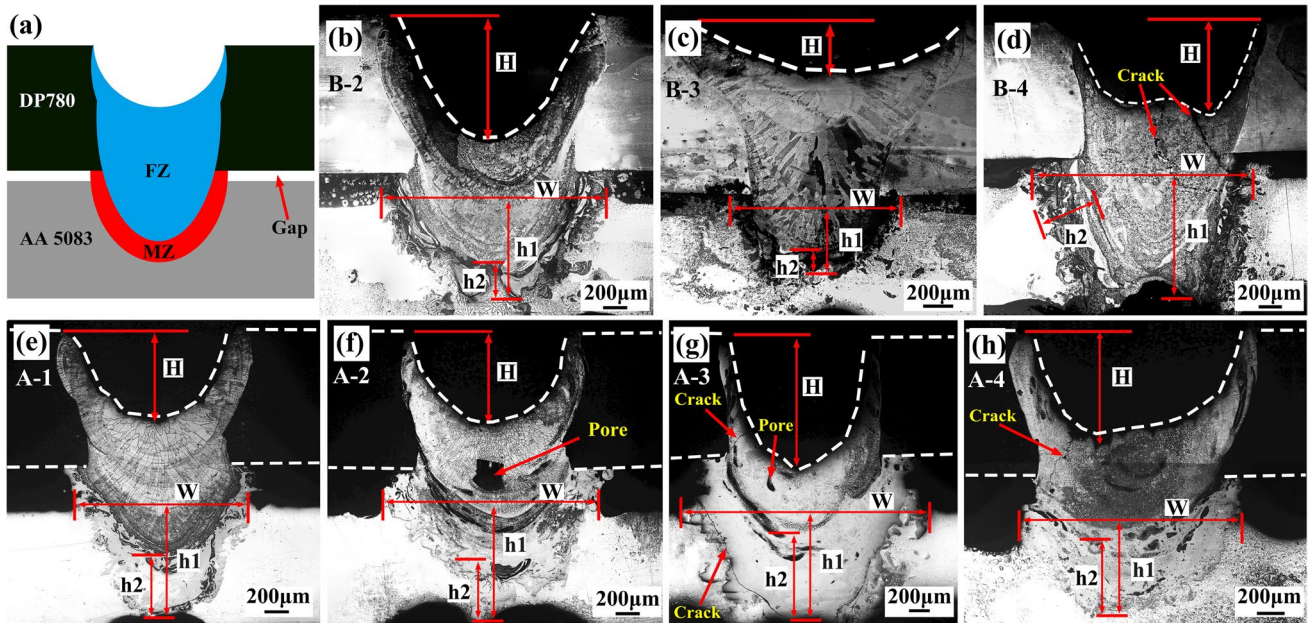


**Fig. 3** The macrostructures on the cross-section of those welded joints: **a** schematic diagram of the cross-section of the joints; **b–d** the joints of Group B; **e–h** the joints of Group A

based on their different morphologies. A schematic diagram of the cross-section of the welded joint is shown in Fig. 3a. The macroscopic morphology and geometric characteristics of various welded joints are presented in Fig. 3b–h. The macroscopic morphologies of various welded joints are unsatisfactory. Crack defects are observed in the FZs and MZs of samples B-4, A-3, and A-4, while porosity defects are seen in the FZs of samples A-2 and A-3. Moreover, the morphologies of banded, blocky, and acicular IMCs are found in the MZs of all the welded joints. These unsatisfactory formations of welded joints may be closely related to the method of laser deposition welding, as well as the welding parameters and filler materials.

Figure 4 reveals the force–displacement characteristics of various welded joints during the shear tests. It is observed that for each test sample, the shear force rapidly decreases once it reaches the maximum value, without any post-yield deformation. It is indicated that the fracture mode is brittle [37]. Figure 4 suggests that the B-2 sample presents the highest force and displacement among the samples in Group B. However, only a small displacement is observed during the shear test for the B-2 sample (~1.4 mm). This reveals that all joints in Group B exhibit poor ductility. On the contrary, the joints in Group A exhibited higher shear force and displacement in the force–displacement curves compared to Group B. Even some samples in Group A have welding defects, such as cracks and porosity (refer to samples A-2 and A-3 in Fig. 3). In particular, the highest shear force is achieved in the A-1 sample (~2013 N), which is ~1.6 times higher than that of the B-2 sample. Moreover, the displacement of the former is ~4.9 mm, which is ~3.5 times higher than the latter. These results validate that the shear properties of Group A joints are superior to those of Group B. Therefore, compared to Al-10Si-0.3 Mg powder, the filler material of FeCoCrNiMn powder may possess more advantages in terms of enhancing
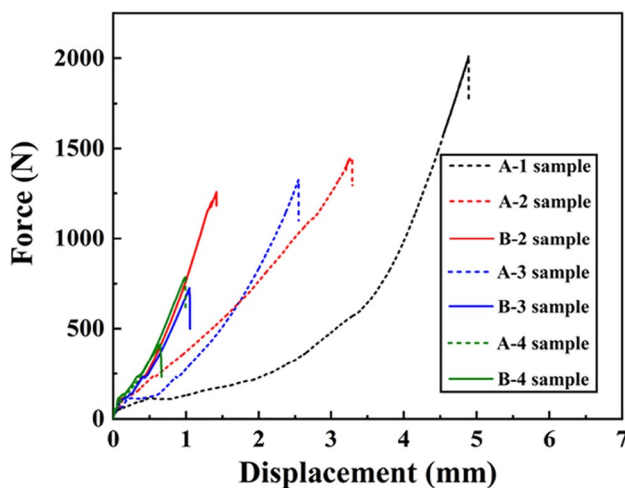


**Fig. 4** The force–displacement behaviors of various welded joints

shear properties. Additionally, as the laser power increases, the shear properties of these joints gradually decrease. This implies that selecting welding parameters with lower heat input is appropriate for achieving dissimilar metal joining of aluminum to steel using laser deposition welding.

## 3.2 Hardness

To analyze the hardness characteristics of the welded joints between DP780 and AA5083, three paths of hardness tests were conducted. The schematic diagram depicting the hardness measuring paths is illustrated by the white arrows in Fig. 5a. Figure 5b presents the hardness values of the welded joints on the steel layer for the A-1 and B-2 samples. The DP780 BM has an average hardness value of ~255 HV. The hardness value increases in the heat-affected zone (HAZ). Both the A-1 and B-2 samples reach their maximum hardness value of ~415 HV in the HAZ. As is known, the HAZ is in an overheated state during the welding process, which may promote the formation of martensite due to rapid cooling, especially for dual-phase steels with both ferrite and martensite [38, 39]. Furthermore, the hardness values of the FZs are higher than that of the DP780 BM. It is noteworthy that the FZ of the A-1 sample has an average hardness value of ~310 HV, which is much lower than that of the B-2 sample (~370 HV). Figure 5c presents the hardness distribution of the FZs along the thickness direction, utilizing the hardness measuring path of c in Fig. 5a, for the A-1 and B-2 samples. It is indicated that the FZ in the A-1 sample exhibits lower hardness compared to the B-2 sample.

Figure 5d exhibits the hardness evolution on the cross-section of the welded joints in the aluminum layer for the A-1 and B-2 samples. The AA 5083 BM has an average value of ~70 HV. The hardness is rarely changed in the HAZ on the AA5083 layer. Moreover, an extremely high hardness of ~1180 HV can be found in the MZ of the B-1 sample, while the maximum hardness in the MZ of the A-1 sample is ~565 HV. The results reveal that the FeCoCrNiMn powder may result in a lower hardness value in the MZ for the dissimilar welded joints of AA5083 to DP780, compared to the Al-10Si-0.3 Mg powder. According to previous studies, great differences in hardness values are presented in different types of Fe-Al IMCs [22, 33, 36]. Al-rich IMCs typically exhibit hardness values of ~800–1100 HV, while Fe-rich IMCs exhibit hardness values of ~350–500 HV. Based on the hardness values in the MZs of two welded joints, it can be inferred that different types of Fe-Al IMCs may be formed in the MZs.

Figure 5e illustrates the average hardness values of the FZs for various dissimilar welded joints, including Groups A and B. The hardness variation in the FZs with the laser power changes can be observed. Figure 5e indicates that only a few changes in hardness values can be found in the FZs of Group A. The A-1 sample shows the lowest value of ~310
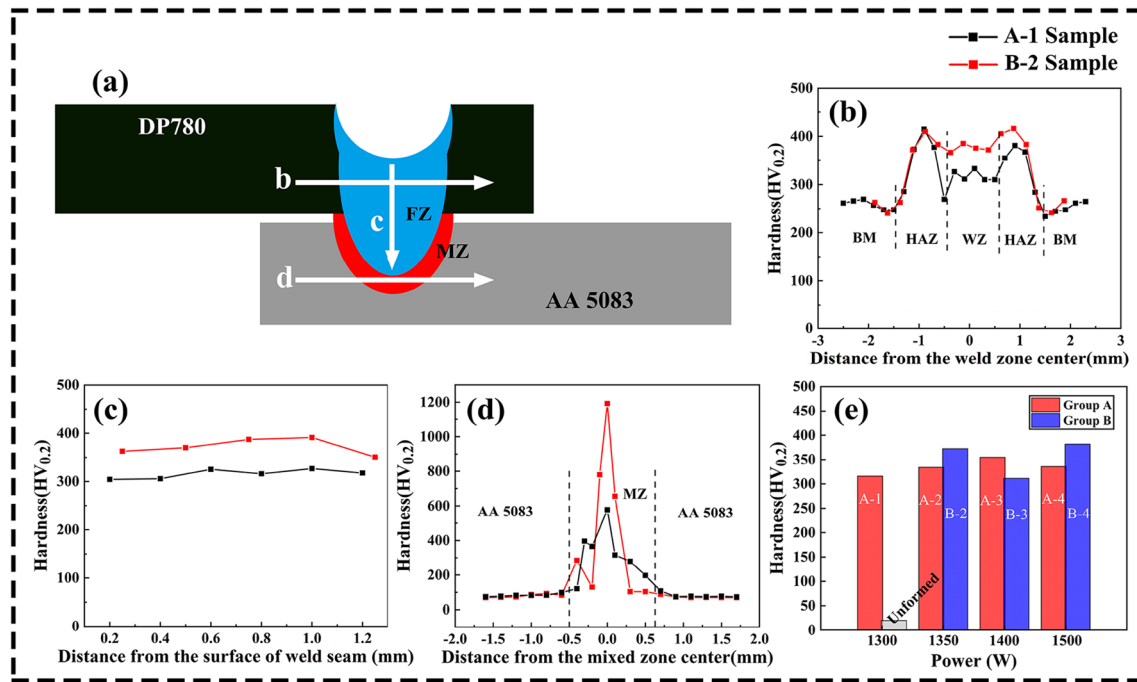
**Fig. 5** The hardness of various dissimilar welded joints: **a** the schematic diagram of hardness measuring paths; **b–d** hardness evolutions for the A-1 and B-2 samples; **e** the average hardness values of the FZs for various dissimilar welded joints

HV, while the A-3 sample has the highest value of ~355 HV. In Group B, the B-4 sample presents the highest value of ~380 HV. The results indicate that, overall, the hardness value of the FZ in Group A is lower than that of Group B. This means that compared to using the Al-10Si-0.3 Mg powder, the weld metals using the FeCoCrNiMn powder would exhibit a lower hardness value.

## 3.3 Microstructure

As described above, the A-1 and B-2 samples have promising welding formation and demonstrate the best shear properties within their respective groups. Therefore, the microstructure analysis focuses on these two samples. The microstructure evolution of the WZs is presented in Fig. 6. In the A-1 sample, columnar grains are mainly observed in the FZ (Fig. 6a). The average primary arm spacing of the columnar grains is ~43.0 μm. Differently, the microstructure of the FZ in the B-2 sample consists mainly of equiaxed grains (Fig. 6d). The average grain size of the equiaxed grains in the FZ center is ~24.5 μm. Figure 6b exhibits the morphologies of belt-like and acicular structures in the MZ of the A-1 sample, which are significantly different from those in the FZ of the same sample. It means that macrosegregation, caused by material flow during the welding process, particularly in dissimilar metal welding [40], is presented in the MZ. The MZ has a different chemical composition, phase composition, and structure, compared to

the FZ. The high magnification of the acicular structures is presented in Fig. 6c. The acicular structures, with an average length of ~27.0 μm, are distributed between two belt-like structures. Similar acicular and belt-like structures are also found in the MZ of the B-2 sample (Fig. 6e). And the size of acicular structures in the MZ of the B-2 sample (~57.8 μm) is ~2.1 times that of the A-1 sample.

SEM images of the microstructure in the WZ of the A-1 sample are presented in Fig. 7. The elemental compositions of the various microstructures were investigated using EDS point analysis, and the measured points are indicated in Fig. 7. The possible phases have been listed based on the elemental composition, as shown in Table 2. Figure 7a illustrates that Points 1 and 2 are located at the interior and boundary of the columnar grains in the FZ, respectively. It has been found that the primary elements in the FZ are Fe and Al, along with small amounts of Cr, Mn, and Co elements. The segregation of Fe and Al elements is presented, resulting in the formation of various Fe-Al phases in the weld metal. However, no segregation of other elements is observed due to the low content of the Cr, Mn, and Co elements. The contents of Fe and Al elements for Points 1 and 2 are ~84 at.% and ~13 at.%, respectively. Based on the phase diagram of the Fe-Al binary alloy [41, 42], the Al element may exist in α-Fe as a solid solution and does not form the Fe-Al phase when the Al content is less than 22.2 at.%. Therefore, the possible phase of the columnar grains in the FZ of the A-1 sample is α-Fe. The measured Points 3 and
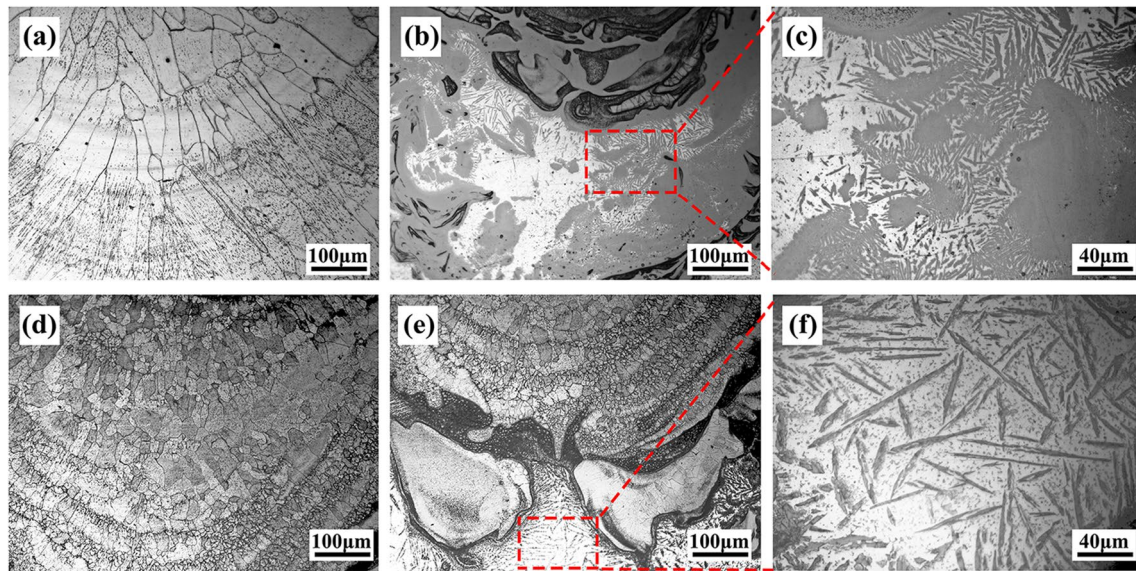
**Fig. 6** Microstructure evolution of the WZs. **a** The FZ of A-1 sample. **b**, **c** The MZ of A-1 sample. **d** The FZ of B-2 sample. **e**, **f** The MZ of B-2 sample

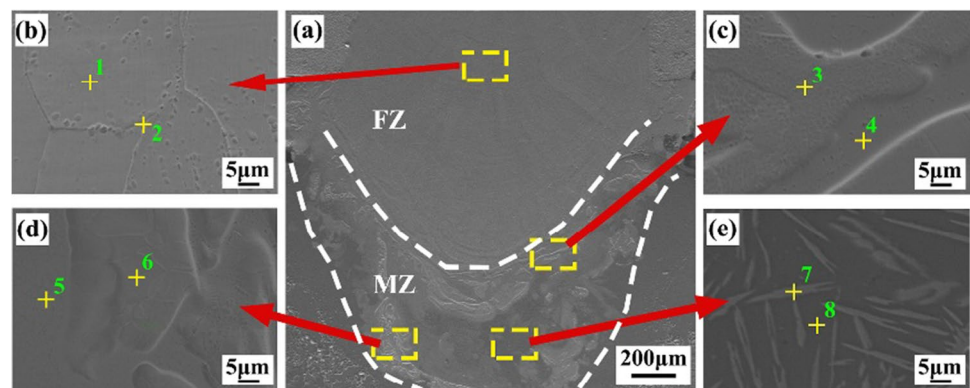**Fig. 7** SEM and EDS point analysis of the microstructure in the WZ of the A-1 sample



**Table 2** Element content (at.%) in the measured points of the A-1 sample

| Measured points | Fe | Al | Mn | Cr | Mg | Possible phase |
|---|---|---|---|---|---|---|
| 1 | 84.21 | 12.67 | 2.01 | 1.11 | - | α-Fe |
| 2 | 83.37 | 13.41 | 1.98 | 1.25 | - | α-Fe |
| 3 | 80.49 | 15.66 | 2.27 | 1.58 | - | α-Fe |
| 4 | 62.97 | 33.65 | 2.18 | 1.21 | - | Fe$_3$Al |
| 5 | 44.79 | 52.09 | 1.80 | 1.32 | - | FeAl |
| 6 | 82.35 | 13.71 | 2.49 | 1.45 | - | α-Fe |
| 7 | 20.18 | 78.03 | 1.24 | 0.54 | - | Fe$_4$Al$_{13}$ |
| 8 | 0.25 | 93.74 | - | - | 6.01 | α-Al |

6 are located at the belt-like structures in the MZ. Table 2 indicates that structures with convex morphologies have a similar elemental composition to Points 1 and 2. This means that the possible phase at the convex structures in the MZ should be α-Fe. Moreover, the Al content for Points 4 and

5, located in the structures with concave morphologies, has increased to 33~52 at.%. Based on the phase diagram of the Fe-Al binary alloy, the Fe$_3$Al phase can be generated when the Al content is 22.2~36.5 at.%, while the FeAl phase can be formed at 22.0~54.5 at.%. Therefore, the possible

phases of the structures with concave morphologies in the MZ should be $Fe_3Al$ and FeAl. For the acicular structures in the MZ, Table 2 reveals that the Al element reaches ~78 at.% (see Point 7). The possible phase of the acicular structures may be $Fe_4Al_{13}$ based on the phase diagram as well as previous studies [41, 43, 44].

EBSD is adopted to obtain more detailed information about the microstructure in the WZ of the A-1 sample. The phase maps of the FZ and MZ, measured by EBSD, are illustrated in Fig. 8. The α-Fe phase is presented in the FZ of the A-1 sample, which is consistent with the EDS analysis results. Moreover, three phases of α-Fe, $Fe_2Al_5$, and $Fe_4Al_{13}$ are detected in the MZ. The acicular structures are $Fe_4Al_{13}$ phase, which is well consistent with the EDS analysis. In addition, the grain boundary image (GB), IPF, KAM, and misorientation angle distribution of the FZ and MZ of the A-1 sample are exhibited in Fig. 9. It can be observed that the grain size gradually refines from the FZ to the MZ. The grain morphologies are transformed from columnar to equiaxed grains. The IPFs of the FZ and the MZ in Fig. 9a and b indicate that the color distribution of the grains is relatively scattered. This means that the texture is rarely presented in the WZ [45]. Comparing the KAM maps of the FZ and MZ in Fig. 9a and b, it is evident that the KAM values of the MZ are higher than those of the FZ [46, 47]. The misorientation angle distribution (Fig. 9c, d) exhibits that the fraction of low-angle boundaries (2~10°) in the MZ (~6.9%) is largely decreased compared to that of the FZ (~27.6%). The fraction of the misorientation angle of 30~60° is a significant decrease from ~77.2% in the FZ to ~44.6% in the MZ. The results indicate that the MZ should have more recrystallized grains compared to the FZ [48].

SEM images of the microstructure in the WZ of the B-2 sample, and the EDS-measured points, are indicated in Fig. 10. The results are presented in Table 3. It is observed that the microstructure morphologies in the WZ of the B-2 sample are more complex compared to those in the A-1 sample. Figure 10 indicates that equiaxed dendrites are found on the top of the FZ for the B-2 sample. Equiaxed grains appear

in the middle of the FZ. Table 3 demonstrates that the main elements of the FZ are Fe and Al, which are similar with those found in the A-1 sample. The contents of Fe and Al elements in the FZ are 69~76 at.% and 22~29 at.% (see Points 1 and 2 in Table 3). This means that the Al content in the FZ of the B-2 sample is much higher than that of the A-1 sample, which may promote the formation of the Fe-Al IMCs in the former, taking the place of the α-Fe phase found in the latter. Moreover, structures with island and acicular morphologies were found in the MZ of the B-2 sample. These structures are clearly distinct from the FZ. It means macrosegregation is also presented in the welded joints when using Al-10Si-0.3 Mg powders [40]. The MZ has a different phase composition and structure compared to the FZ. Therefore, EDS analysis was conducted on these structures. Table 3 shows that the island structure has a low Al element content of ~19.7 at.% (Point 3), which is much lower than that of the acicular structure (~79.3 at.%) (Point 5). Based on the phase diagram of the Fe-Al binary alloy [41, 42], the possible phase for island morphology is α-Fe, and that of the acicular structure is $Fe_4Al_{13}$. The microstructure between the island and the acicular structures has an Al element content of ~68.4 at.%. It may be $Fe_2Al_5$ (Point 4). Moreover, ravine-like and strip-like structures were also observed in the MZ of the B-2 sample. Table 3 suggests that the ravine-like structure may be FeAl, and the long strip-like structures may be α-Al. The results prove that the phase structure in the weld metal of the B-2 sample is complex.

The XRD patterns of these two WZs are exhibited in Fig. 11. The diffraction peaks $2\theta$ of those two samples are similar on the whole. This means that the types of IMCs in those two WZs are similar. Many types of Fe-Al IMCs, including FeAl, $Fe_2Al_5$, and $Fe_4Al_{13}$, are detected in the WZs, which is well consistent with the analysis mentioned above. Moreover, as described above (Tables 2 and 3), the FZ of the A-1 sample has a lower content of Al element and can promote the formation of α-Fe or a small amount of Fe-Al phase, while that of the B-2 sample has a higher content of Al element and promotes the formation of Fe-Al phase. Due to the increase in the Al content of the MZs,

**Fig. 8** EBSD phase map of the FZ and MZ for the A-1 sample. **a** The FZ. **b** The MZ



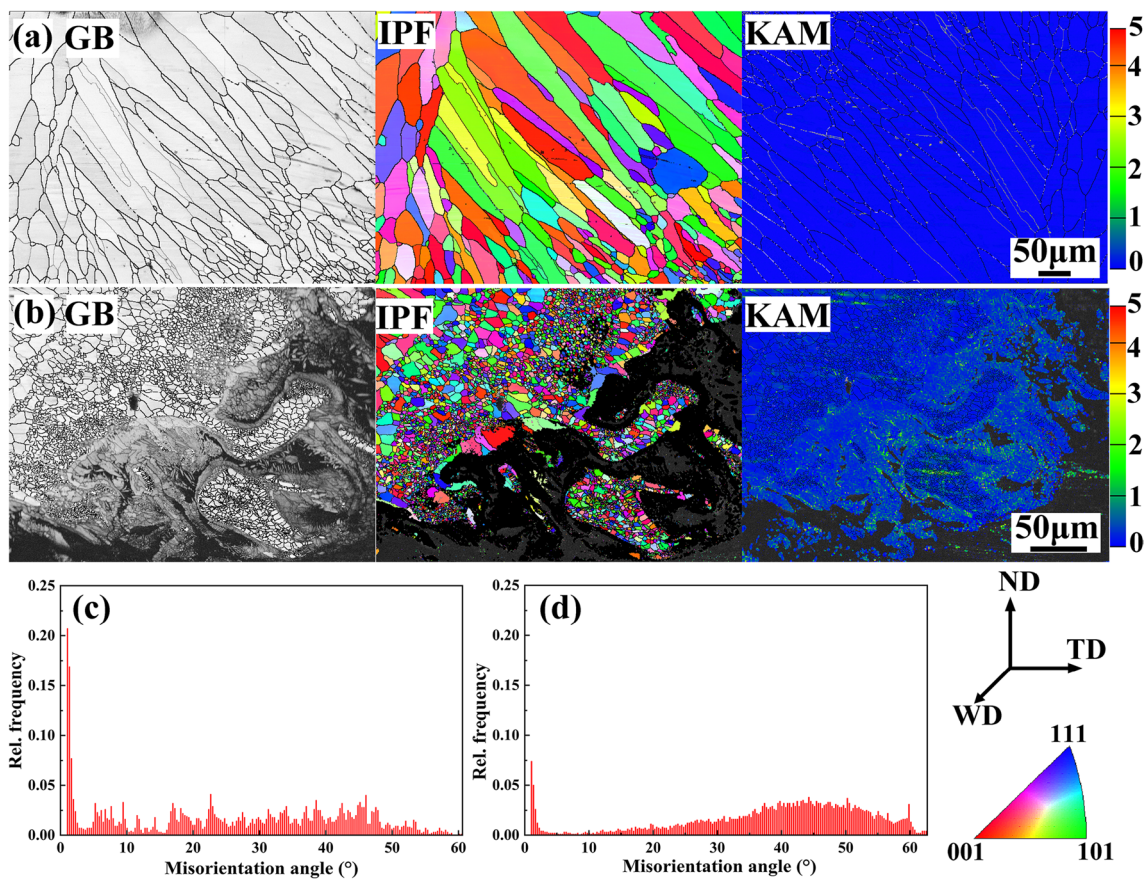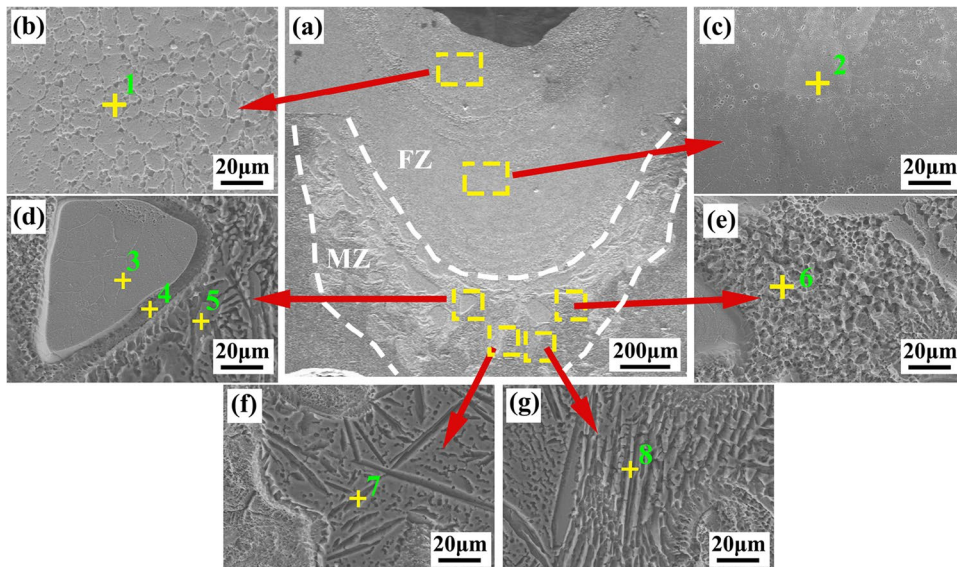Fe-BCC    $Fe_2Al_5$    $Fe_4Al_{13}$
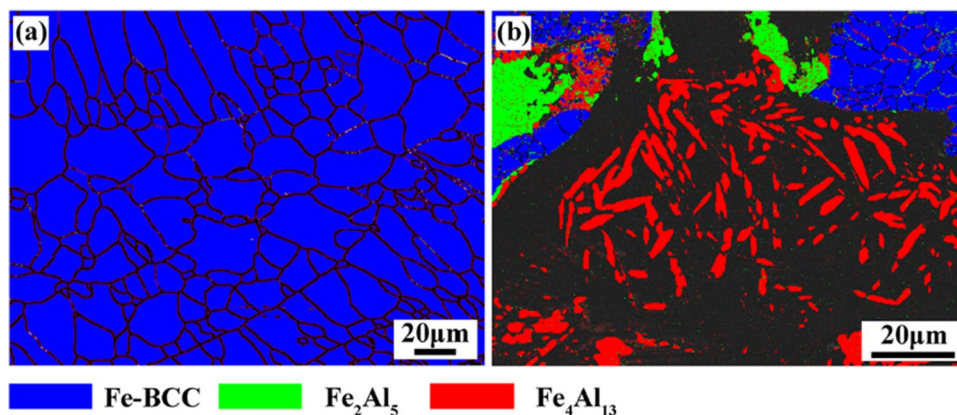
**Fig. 9** EBSD grain boundary image (GB), inverse pole figure (IPF), Kernel average misorientation (KAM), and misorientation angle distribution in the A-1 sample. **a**, **c** The FZ. **b**, **d** The MZ



**Fig. 10** SEM and EDS point analysis of the microstructure in the WZ of the B-2 sample

Al-rich IMCs such as $Fe_2Al_5$ and $Fe_4Al_{13}$ are generated for both the A-1 and B-2 samples. The analysis is confirmed by the EBSD (Fig. 8). Different phase structures have an impact on the hardness and shear properties of the WZs, which will be further discussed in the "Discussion" section.

**Table 3** Element content (at.%) in the measured points of the B-2 sample

| Measured points | Fe | Al | Mn | Mg | Possible phase |
|---|---|---|---|---|---|
| 1 | 69.22 | 29.84 | 0.95 | - | $Fe_3Al$ |
| 2 | 76.24 | 22.83 | 0.93 | - | $\alpha$-Fe + FeAl |
| 3 | 79.20 | 19.72 | 1.09 | - | $\alpha$-Fe |
| 4 | 31.25 | 68.36 | 0.39 | - | $Fe_2Al_5$ |
| 5 | 17.73 | 79.26 | 1.07 | 1.94 | $Fe_4Al_{13}$ |
| 6 | 54.11 | 45.16 | 0.73 | - | FeAl |
| 7 | 0.34 | 94.96 | - | 4.69 | $\alpha$-Al |
| 8 | 0.46 | 94.27 | - | 5.26 | $\alpha$-Al |
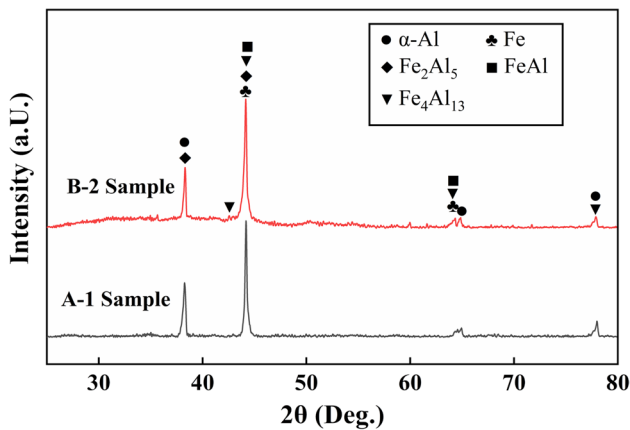


**Fig. 11** XRD patterns of the WZs for the A-1 and B-2 samples

## 4 Discussion

### 4.1 Influence of laser power on geometric parameters

As described in Fig. 3, various weld morphologies, including weld collapse, FZ, and MZ, are observed in the welded joints. To further investigate the morphological variation of the WZs corresponding to different laser powers, several parameters were roughly measured, including the depth of weld collapse ($H$), the maximum melting width of the aluminum layer ($W$), the penetration depth of the aluminum layer ($h1$), and the maximum thickness of the MZ ($h2$). The results are summarized in Table 4. In Group A samples, it is observed that the value of $H$ increases as the laser power increases. In Group B samples, the values of $H$ initially decrease and then increase with increasing laser power. The results indicate that reducing the laser power is beneficial in mitigating weld collapse.

To further clarify the influence of laser power on the geometric characteristics of the WZs, geometric parameters of $\varphi$ and $\lambda$ are proposed and calculated. The geometric parameters of $\varphi$ and $\lambda$ can be calculated according to the following equation:

$$\varphi = \frac{W}{h1} \tag{1}$$

$$\lambda = \frac{h2}{h1} \tag{2}$$

The parameter of $\varphi$ indicates the width-depth ratio of the WZ on the aluminum layer, describing the state of weld formation on the aluminum layer. On the other hand, the parameter of $\lambda$ implies the proportion of the MZ to the WZ on the aluminum layer. The results in Table 4 and Fig. 12 indicate that for Group A, the geometric parameters of $\varphi$ and $\lambda$ are positively correlated with laser power. This suggests that the welded joint tends to form a narrow and deep WZ with a relatively small proportion of MZ when the laser power is low. For Group B, the variation of $\lambda$ is similar with that of Group A. The parameter of $\varphi$ increases first and then decreases with the increase of laser power. It implies that the laser power has a significant effect on the geometric characteristics of the welded joints when using Al-10Si-0.3 Mg powder. Based on the experimental results, a high $\varphi$ parameter can lead to cracks in the WZ, which can also deteriorate the shear properties of the welded joints. It means that the appropriate parameters are important for the weld formation of Al/steel joints when using laser deposition welding. In addition, Fig. 12 shows

**Table 4** The geometric parameters of WZs for those welded joints

| Samples | Geometric parameters | | | | | |
|---|---|---|---|---|---|---|
| | $H$ (μm) | $W$ (μm) | $h1$ (μm) | $h2$ (μm) | $\varphi$ | $\lambda$ (%) |
| A-1 | 775 | 1414 | 926 | 515 | 1.53 | 55.6 |
| A-2 | 798 | 1762 | 948 | 512 | 1.86 | 54.1 |
| A-3 | 1342 | 2343 | 1016 | 825 | 2.31 | 81.3 |
| A-4 | 845 | 1583 | 687 | 554 | 2.31 | 80.7 |
| B-2 | 954 | 1838 | 811 | 304 | 2.27 | 37.5 |
| B-3 | 387 | 1111 | 422 | 156 | 2.63 | 36.8 |
| B-4 | 921 | 1883 | 1057 | 506 | 1.78 | 47.8 |

**Fig. 12** The geometric parameters of the weld formation with the change of the laser power: (**a**) $\varphi$ parameter; (**b**) $\lambda$ parameter
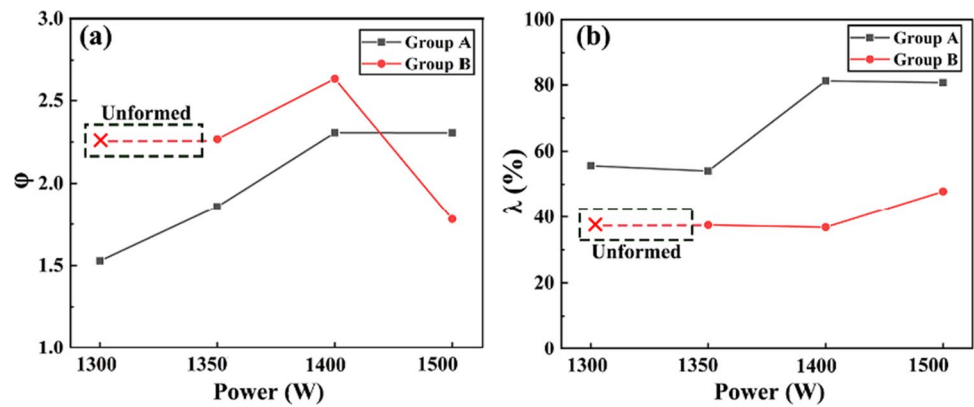
that the type of filler materials can affect the geometric parameters of $\varphi$ and $\lambda$. Compared to the samples of Group B, Group A usually has a smaller value of $\varphi$ and a higher value of $\lambda$ with the same laser power.

Geometric parameters have an impact on the shear properties of dissimilar welded joints [49–51]. Based on the experimental results (Figs. 4 and 12), for both Group A and Group B, an increase in laser power resulted in a gradual increase in the geometrical parameter of $\lambda$ and a decrease in the shear strength of the joints. This suggests that there is a significant correlation between the shear properties of the welded joints and the $\lambda$ parameter. As described above, many $Fe_2Al_5$ and $Fe_4Al_{13}$ IMCs are present in the MZ (Figs. 7, 8, and 10). The increase in the proportion of the MZ can significantly deteriorate the shear properties of the welded joints.

Moreover, an increase in the $\varphi$ parameter is unfavorable to the shear properties, especially for the samples in Group A (Figs. 4 and 12). A high $\varphi$ parameter can lead to cracks in the WZ, which can also deteriorate the shear properties of the welded joints. This means that, for dissimilar metal joining of aluminum to steel using laser deposition welding, it is appropriate to use the welding parameter with low heat input. However, for the multi-principal filler material, many elements with a high melting point, such as Fe, Co, Cr, and Ni, are used [5, 52]. High heat input is required to melt the filler materials. It means that welding parameters with excessively high or low heat input are not suitable for dissimilar welding of aluminum to steel. Therefore, it is imperative to optimize the welding parameters for laser deposition welding of aluminum to steel using a multi-principal filler material.

## 4.2 Relationship between microstructure and mechanical properties

Figure 11 reveals that multiple types of Fe-Al IMCs are detected in the WZs for both the A-1 and B-2 samples. The results demonstrate that the multi-principal filler material of FeCoCrNiMn was unable to fully prevent the formation of Fe-Al IMCs in the weld metal during the laser lap welding

of aluminum to steel. This finding is different from previous studies, which reported that the high-entropy effect could significantly inhibit the formation of Fe-Al IMCs in the WZ when using FeCoCrNiMn filler material [33, 34]. In this study, the steel is arranged on the top, and the aluminum is arranged on the bottom. This means that the filler material powder is deposited and mixed onto the upper steel layer, which has minimal contact with the lower aluminum layer. Therefore, it has not hindered the formation of Fe-Al IMCs, which are mainly found in the MZ, close to the aluminum layer.

Figure 11 indicates that the types of IMCs in the weld metals of the two samples are similar. For the A-1 sample, the FZ mainly consists of the Fe-BCC phase without the Fe-Al phase, while the MZ predominantly contains a fine acicular $Fe_4Al_{13}$ phase and a small amount of $Fe_2Al_5$ phase. However, for the B-2 sample, the FZ contains a significant amount of IMCs such as $Fe_3Al$ and FeAl. Moreover, the predominant Al-rich Fe-Al phases, specifically $Fe_2Al_5$ and $Fe_4Al_{13}$, are presented in the MZ. As is known, Al-rich IMCs have higher hardness and lower plasticity compared to Fe-rich IMCs in Fe-Al phases. Increasing the proportion of the Fe-rich phase in the weld metal can improve the mechanical properties of the Al/steel joint, compared to Al-rich IMCs [53, 54].

Based on the experimental results (Tables 2 and 3), the filler material of FeCoCrNiMn may prevent the migration of the Al element from the bottom to the upper WZ. As a result, the FZ of the A-1 sample has a lower content of Al element, which can promote the formation of $\alpha$-Fe or a small amount of Fe-Al phase (Fig. 8). However, the B-2 sample has a higher content of Al element, which promotes the formation of Fe-Al phases in the FZ. Moreover, Fig. 6 shows that the grain size of the FZ in the A-1 sample is larger than that of the B-2 sample. However, Fig. 5 indicates that a higher hardness is observed in the FZ of the B-2 sample, compared to the A-1 sample. It means that the phase structures, especially those of Fe-Al IMCs, contribute to the higher hardness in the FZ of the B-2 sample. In addition, Fig. 6 shows that the size of Fe-Al IMCs (acicular structures) in the MZ of the B-2 sample is ~2.1 times that of the A-1 sample. It may be another reason for the higher hardness in the FZ

and lower shear properties of the B-2 sample, compared to the A-1 sample. Therefore, when compared to the Al-10Si-0.3 Mg powder, the FeCoCrNiMn powder offers several advantages in terms of reducing the hardness and improving the shear properties of the laser lap welding of AA 5083 to DP780 steel.

## 5 Conclusions

(1) The use of FeCoCrNiMn as a multi-principal filler material was unable to prevent the formation of Fe-Al IMCs in the weld metal during the laser lap welding of AA 5083 to DP780 steel. Many Fe-Al IMCs were detected in the weld zone, particularly in the mixed zone.

(2) The use of FeCoCrNiMn powder would result in coarse columnar grains in the upper fusion zone, replacing the equiaxed grains found in the joints made with Al-10Si-0.3 Mg powder.

(3) Compared to the Al-10Si-0.3 Mg powder, the FeCoCrNiMn filler material had advantages in reducing the hardness of the weld zone and improving the shear properties of the lap welded joints of AA 5083 to DP780 steel.

(4) Selecting welding parameters with a low heat input was appropriate for dissimilar metal joining of aluminum to steel using laser deposition welding.

## Declarations

**Competing interests** The authors declare no competing interests.

## References

1. Hong KM, Shin YC (2017) Prospects of laser welding technology in the automotive industry: a review. J Mater Process Technol 245:46–69. https://doi.org/10.1016/j.jmatprotec.2017.02.008

2. Sadeghian A, Iqbal N (2022) A review on dissimilar laser welding of steel-copper, steel-aluminum, aluminum-copper, and steel-nickel for electric vehicle battery manufacturing. Opt Laser Technol 146:107595. https://doi.org/10.1016/j.optlastec.2021.107595

3. Xie J, Cai C, Zhang B, Yu J, Liu Y (2023) Microstructure evolution and fracture behavior of rotating laser welded-brazed 6061 aluminum alloys/304 SS dissimilar joint. Mater Charact 195:112543. https://doi.org/10.1016/j.matchar.2022.112543

4. Yang J, Su J, Gao C, Zhao Y, Liu H, Oliveira JP, Tan C, Yu Z (2021) Effect of heat input on interfacial microstructure, tensile and bending properties of dissimilar Al/steel lap joints by laser welding-brazing. Opt Laser Technol 142:107218. https://doi.org/10.1016/j.optlastec.2021.107218

5. Zheng M, Yang J, Xu J, Jiang J, Zhang H, Oliveira JP, Lv X, Xue J, Li Z (2023) Interfacial microstructure and strengthening mechanism of dissimilar laser al/steel joint via a porous high entropy alloy coating. J Mater Res Technol 23:3997–4011. https://doi.org/10.1016/j.jmrt.2023.02.040

6. Zhao Y, Long Y, Li Z (2022) Research progress of transition layer and filler wire for laser welding of steel and aluminum dissimilar metals. Int J Adv Manuf Technol 119:4149–4158. https://doi.org/10.1007/s00170-021-08442-z

7. Li M, Tao W, Zhang J, Wang Y, Yang S (2022) Hybrid resistance-laser spot welding of aluminum to steel dissimilar materials: microstructure and mechanical properties. Mater Des 221:111022. https://doi.org/10.1016/j.matdes.2022.111022

8. Li T, Zhou D, Yan Y, Zhang S, Liu J (2020) Effect of Ti foil on microstructure and mechanical properties of laser fusion welding of DP590 dual-phase steel to 6022 aluminum alloy. Mater Sci Eng A 796:139929. https://doi.org/10.1016/j.msea.2020.139929

9. Yang J, Oliveira JP, Li Y, Tan C, Gao C, Zhao Y, Yu Z (2022) Laser techniques for dissimilar joining of aluminum alloys to steels: a critical review. J Mater Process Technol 301:117443. https://doi.org/10.1016/j.jmatprotec.2021.117443. (ARTN117443)

10. Shi L, Kang J, Qian C, Liang J, Shalchi-Amirkhiz B, Haselhuhn AS, Carlson BE (2021) Role of $Fe_2Al_5$ in fracture of novel dissimilar aluminum-steel resistance spot welds using multi-ring domed electrodes. Mater Sci Eng A 831:142233. https://doi.org/10.1016/j.msea.2021.142233

11. Cui L, Chen B, Qian W, He D, Chen L (2017) Microstructures and mechanical properties of dissimilar Al/steel butt joints produced by autogenous laser keyhole welding. Metals 7(11):492. https://doi.org/10.3390/met7110492. (ARTN 492)

12. Li L, Xia H, Tan C, Ma N (2018) Influence of laser power on interfacial microstructure and mechanical properties of laser welded-brazed Al/steel dissimilar butted joint. J Manuf Process 32:160–174. https://doi.org/10.1016/j.jmapro.2018.02.002

13. Mukherjee M, Kundu J, Shome M (2022) Effect of processing parameters on the interface characteristics and joint strengths of aluminum-on-steel lap joints produced using conduction mode laser welding. Weld World 66:2461–2482. https://doi.org/10.1007/s40194-022-01392-4

14. Shu F, Niu S, Zhu B, Wu L, Xia H, Chen B, Zhao J, Tan C (2021) Effect of pulse frequency on the nanosecond pulsed laser welded Al/steel lapped joint. Opt Laser Technol 143:107355. https://doi.org/10.1016/j.optlastec.2021.107355

15. Yu X, Fan D, Huang J, Li C, Kang Y (2019) Arc-assisted laser welding brazing of aluminum to steel. Metals 9(4):397. https://doi.org/10.3390/met9040397

16. Peng M, Liu H, Liang Y, Xu W, Zhao Y, Chen S, Weng J, Yang J (2022) CMT welding-brazing of al/steel dissimilar materials using cycle-step mode. J Mater Res Technol 18:1267–1280. https://doi.org/10.1016/j.jmrt.2022.03.043

17. Li T, Zhou D, Yan Y, Liu J (2021) Effect of laser-Ti foil coupling on microstructure and mechanical property of steel/aluminum

fusion welding joints. Opt Laser Technol 141:107114. https://doi.org/10.1016/j.optlastec.2021.107114

18. Zhang Y, Guo G, Li F, Wang G, Wei H (2017) The interface control of butt joints in laser braze welding of aluminum-steel with coaxial powder feeding. J Mater Process Technol 246:313–320. https://doi.org/10.1016/j.jmatprotec.2017.03.020

19. Su J, Yang J, Li Y, Yu Z, Chen J, Zhao W, Liu H, Tan C (2020) Microstructure and mechanical properties of laser fusion welded Al/steel joints using a Zn-based filler wire. Opt Laser Technol 122:105882. https://doi.org/10.1016/j.optlastec.2019.105882

20. Yuan R, Deng S, Cui H, Chen Y, Lu F (2019) Interface characterization and mechanical properties of dual beam laser welding-brazing Al/steel dissimilar metals. J Manuf Process 40:37–45. https://doi.org/10.1016/j.jmapro.2019.03.005

21. Ye Z, Huang J, Cheng Z, Wang S, Yang J, Chen S, Zhao X (2021) Interfacial characteristics and mechanical properties of aluminum/steel butt joints fabricated by a newly developed high-frequency electric cooperated arc welding-brazing process. J Mater Process Technol 298:117317. https://doi.org/10.1016/j.jmatprotec.2021.117317

22. Yang J, Li Y, Zhang H (2016) Microstructure and mechanical properties of pulsed laser welded Al/steel dissimilar joint. Trans Nonferr Metal Soc 26(4):994–1002. https://doi.org/10.1016/S1003-6326(16)64196-1

23. Xia H, Zhao X, Tan C, Chen B, Song X, Li L (2018) Effect of Si content on the interfacial reactions in laser welded-brazed Al/steel dissimilar butted joint. J Mater Process Technol 258:9–21. https://doi.org/10.1016/j.jmatprotec.2018.03.010

24. Yuce C, Karpat F, Yavuz N (2019) Investigations on the microstructure and mechanical properties of laser welded dissimilar galvanized steel–aluminum joints. Int J Adv Manuf Technol 104(5–8):2693–2704. https://doi.org/10.1007/s00170-019-04154-7

25. Chen S, Zhai Z, Huang J, Zhao X, Xiong J (2016) Interface microstructure and fracture behavior of single/dual-beam laser welded steel-Al dissimilar joint produced with copper interlayer. Int J Adv Manuf Technol 82:631–643. https://doi.org/10.1007/s00170-015-7390-x

26. Suzuki KT, Omura S, Tokita S, Sato YS, Tatsumi Y (2023) Drastic improvement in dissimilar aluminum-to-steel joint strength by combining positive roles of silicon and nickel additions. Mater Des 225:111444. https://doi.org/10.1016/j.matdes.2022.111444

27. Tan C, Zang C, Xia H, Zhao X, Zhang K, Meng S, Chen B, Song X, Li L (2018) Influence of Al additions in Zn–based filler metals on laser welding–brazing of Al/steel. J Manuf Process 34:251–263. https://doi.org/10.1016/j.jmapro.2018.06.008

28. Wu D, Li H, Yang Y, Cai X, Wang L, Sun D (2022) Plasma arc welding of dissimilar ultrahigh-strength steel and aluminum alloy assisted by copper transition layer. Mater Lett 318:132202. https://doi.org/10.1016/j.matlet.2022.132202

29. Xu T, Zhou S, Wu H, Hong C, Ma X (2022) Effect of nickel interlayer thickness on lap joint laser welding for aluminum-steel dissimilar materials. Sci Technol Weld Join 27(3):166–175. https://doi.org/10.1080/13621718.2022.2026066

30. Shen J, Gonçalves R, Choi YT, Lopes JG, Yang J, Schell N, Kim HS, Oliveira JP (2023) Microstructure and mechanical properties of gas metal arc welded CoCrFeMnNi joints using a 308 stainless steel filler metal. Scr Mater 222:115053. https://doi.org/10.1016/j.scriptamat.2022.115053

31. Shen J, Gonçalves R, Choi YT, Lopes JG, Yang J, Schell N, Kim HS, Oliveira JP (2022) Microstructure and mechanical properties of gas metal arc welded CoCrFeMnNi joints using a 410 stainless steel filler metal. Mater Sci Eng A 857:144025. https://doi.org/10.1016/j.msea.2022.144025

32. Oliveira JP, Shamsolhodaei A, Shen J, Lopes JG, Gonçalves RM, Ferraz MDB, Piçarra L, Zeng Z, Zhou N, Kim HS (2022) Improving the ductility in laser welded joints of CoCrFeMnNi high entropy alloy to 316 stainless steel. Mater Des 219:110717. https://doi.org/10.1016/j.matdes.2022.110717

33. Zhou H, Gu X, Gu X, Dong J, Xu G (2022) Improvement in microstructure and mechanical properties of laser welded steel/aluminum alloy lap joints using high-entropy alloy interlayer. J Mater Res Technol 20:139–146. https://doi.org/10.1016/j.jmrt.2022.07.063

34. Liu D, Wang J, Xu M, Jiao H, Tang Y, Li D, Zhao L, Han S (2020) Evaluation of dissimilar metal joining of aluminum alloy to stainless steel using the filler metals with a high-entropy design. J Manuf Process 58:500–509. https://doi.org/10.1016/j.jmapro.2020.08.031

35. Yan F, Wang X, Chai F, Ma H, Tian L, Du X, Wang C, Wang W (2019) Improvement of microstructure and performance for steel/Al welds produced by magnetic field assisted laser welding. Opt Laser Technol 113:164–170. https://doi.org/10.1016/j.optlastec.2018.12.030

36. Indhu R, Soundarapandian S, Vijayaraghavan L (2018) Yb:YAG laser welding of dual phase steel to aluminum alloy. J Mater Process Technol 262:411–421. https://doi.org/10.1016/j.jmatprotec.2018.05.022

37. Zhang D, Qin G, Ma H, Geng P (2021) Non-uniformity of intermetallic compounds and properties in inertia friction welded joints of 2A14 Al alloy to 304 stainless steel. J Manuf Process 68:834–842. https://doi.org/10.1016/j.jmapro.2021.06.019

38. Alaeibehmand S, Mirsalehi SE, Ranjbarnodeh E (2021) Pinless FSSW of DP600/Zn/AA6061 dissimilar joints. J Mater Res Technol 15:996–1006. https://doi.org/10.1016/j.jmrt.2021.08.071

39. Indhu R, Tak M, Vijayaraghavan L, Soundarapandian S (2020) Microstructural evolution and its effect on joint strength during laser welding of dual phase steel to aluminum alloy. J Manuf Process 58:236–248. https://doi.org/10.1016/j.jmapro.2020.08.004

40. Teshome FB, Peng B, Oliveira JP, Shen J, Ao S, Li H, Chen L, Tan C, Song X, Zhou N, Zeng Z (2023) Role of Pd interlayer on NiTi to Ti6Al4V laser welded joints: microstructural evolution and strengthening mechanisms. Mater Des 228:111845. https://doi.org/10.1016/j.matdes.2023.111845

41. Wang C, Cui L, Mi G, Jiang P, Shao X, Rong Y (2017) The influence of heat input on microstructure and mechanical properties for dissimilar welding of galvanized steel to 6061 aluminum alloy in a zero-gap lap joint configuration. J Alloy Compd 726:556–566. https://doi.org/10.1016/j.jallcom.2017.08.015

42. Zhang D, Qin G, Geng P, Ma H (2021) Study of plastic flow on intermetallic compounds formation in friction welding of aluminum alloy to stainless steel. J Manuf Process 64:20–29. https://doi.org/10.1016/j.jmapro.2021.01.019

43. Pouranvari M (2017) Critical assessment 27: dissimilar resistance spot welding of aluminum/steel: challenges and opportunities. Mater Sci Technol 33(15):1705–1712. https://doi.org/10.1080/02670836.2017.1334310

44. Dinda SK, Das D, Mohan A, Srirangam P, Roy GG (2021) Effect of beam oscillation on electron beam butt welded dual-phase (DP600) steel to 5754 aluminum alloy joints. Metall Mater Trans A 52(5):1723–1731. https://doi.org/10.1007/s11661-021-06181-0

45. Rodríguez-Barber I, Fernández-Blanco AM, Unanue-Arruti I, Madariaga-Rodríguez I, Milenkovic S, Pérez-Prado MT (2023) Laser powder bed fusion of the Ni superalloy Inconel 939 using pulsed wave emission. Mater Sci Eng A 870:144864. https://doi.org/10.1016/j.msea.2023.144864

46. Shen J, Agrawal P, Rodrigues TA, Lopes JG, Schell N, He J, Zeng Z, Mishra RS, Oliveira JP (2023) Microstructure evolution and mechanical properties in a gas tungsten arc welded $Fe_{42}Mn_{28}Co_{10}Cr_{15}Si_5$ metastable high entropy alloy. Mater Sci Eng A 867:144722. https://doi.org/10.1016/j.msea.2023.144722

47. Shen J, Agrawal P, Rodrigues TA, Lopes JG, Schell N, Zeng Z, Mishra RS, Oliveira JP (2022) Gas tungsten arc welding of

as-cast AlCoCrFeNi$_{2.1}$ eutectic high entropy alloy. Mater Des 223:111176. https://doi.org/10.1016/j.matdes.2022.111176

48. Bugajska M, Maj L, Jarzebska A, Terlicka S, Faryna M, Szulc Z et al (2022) Variety of aluminum/steel interface microstructures formed in explosively welded clads followed by the weld's thermal expansion response. J Mater Eng Perform 31:7088–7097. https://doi.org/10.1007/s11665-022-07027-5

49. Tao P, Zhang X, Mi G, Wang C (2023) Research on fiber laser welding formation, microstructure, and mechanical properties of 7.5mm 304 stainless steel. J Mater Res Technol 24:236–249. https://doi.org/10.1016/j.jmrt.2023.02.200

50. Yu J, Cai C, Xie J, Huang J, Liu Y, Chen H (2023) Weld formation, arc behavior, and droplet transfer in narrow-gap laser-arc hybrid welding of titanium alloy. J Manuf Process 91:44–52. https://doi.org/10.1016/j.jmapro.2023.02.022

51. Liu Z, Li X, Pan L, Gao J, Zhang K (2023) Effects of weld penetration modes on laser welding characteristics of a novel ultra-high strength steel for aerospace application. J Manuf Process 90:111–124. https://doi.org/10.1016/j.jmapro.2023.02.003

52. Peng P, Li S, Chen W, Xu Y, Zhang X, Ma Z, Wang J (2022) Phase selection and microhardness of directionally solidified AlCoCrFeNi$_{2.1}$ eutectic high-entropy alloy. Acta Metall Sin-Engl 35:1281–1290. https://doi.org/10.1007/s40195-021-01367-2

53. Cai C, Xie J, Wang H, Chen H (2022) Welding characteristics and mechanical property of rotating laser welding-brazing of aluminum alloy to steel. Opt Laser Technol 151:107989. https://doi.org/10.1016/j.optlastec.2022.107989

54. Xu W, He H, Yi Y, Wang H, Yu C, Fang W (2021) Dissimilar joining of stainless steel and aluminum using twin-wire CMT. Weld World 65(8):1541–1551. https://doi.org/10.1007/s40194-021-01089-0